

Explosion and nucleosynthesis of low redshift pair instability supernovae

A. Kozyreva¹, S.-C. Yoon^{1,2}, and N. Langer¹

¹ Argelander-Institut für Astronomie, Universität Bonn, Auf dem Hügel 71, 53121 Bonn, Germany
e-mail: kozyreva@astro.uni-bonn.de

² Astronomy Program, Department of Physics & Astronomy, Seoul National University, Seoul, 151-742, Republic of Korea

Received XXXXX XX, 2014; accepted XXXXX XX, 2014

ABSTRACT

Context. Both recent observations and stellar evolution models suggest that pair-instability supernovae (PISNe) could occur in the local Universe, at metallicities below $\lesssim Z_{\odot}/3$. Previous PISN models were mostly produced at very low metallicities in the context of the early Universe.

Aims. We present new PISNe models at a metallicity of $Z = 0.001$, which are relevant for the local Universe.

Methods. We take the self-consistent stellar evolutionary models of pair-instability progenitors with initial masses of $150 M_{\odot}$ and $250 M_{\odot}$ at metallicity of $Z = 0.001$ by Langer et al. (2007) and follow the evolution of these models through the supernova explosions, using a hydrodynamics stellar evolution code with an extensive nuclear network including 200 isotopes.

Results. Both models explode as PISNe without leaving a compact stellar remnant. Our models produce a nucleosynthetic pattern that is generally similar to that of Population III PISN models, which is mainly characterized by the production of large amounts of α -elements and a strong deficiency of the odd-charged elements. However, the odd-even effect in our models is significantly weaker than that found in Population III models. The comparison with the nucleosynthetic yields from core-collapse supernovae at a similar metallicity ($Z = 0.002$) indicates that PISNe could have strongly influenced the chemical evolution below $Z \approx 0.002$, assuming a standard initial mass function. The odd-even effect is predicted to be most prominent for the intermediate mass elements between silicon and calcium.

Conclusions. With future observations of chemical abundances in Population II stars, our result can be used to constrain the number of PISNe that occurred during the past evolution of our Galaxy.

Key words. stars: massive – stars: evolution – stars: abundances – stars: supernovae: superluminous supernovae – supernovae: pair instability supernovae – supernovae: general

1. Introduction

The pair instability mechanism for supernova explosions was first suggested in 1960s (Fowler & Hoyle 1964; Bisnovaty-Kogan & Kazhdan 1967; Rakavy & Shaviv 1967; Barkat et al. 1967; Fraley 1968; Zeldovich & Novikov 1971). The cores of very massive stars with initial masses higher than about $100 M_{\odot}$ (Bond et al. 1982; Heger et al. 2003) have relatively low densities and high temperatures for which radiation pressure is dominant over gas pressure. When the core temperature approaches 10^9 K, the creation of electron-positron pairs out of gamma-ray photons from the high energy tail of the black body spectrum becomes important and makes the adiabatic index Γ drop below $4/3$. This causes gravitational collapse of the core if a significant fraction of the core has $\Gamma < 4/3$. The consequent oxygen burning induces a thermonuclear explosion that completely disrupts the star if the released energy exceeds its binding energy. This happens for oxygen core masses above approximately $45 M_{\odot}$.

For a pair instability supernova to occur, its progenitor needs to retain its mass high enough to keep its helium core mass above about $\sim 65 M_{\odot}$. This condition cannot be easily fulfilled at high metallicity for which the evolution of very massive stars are dominated by stellar wind mass-loss (e.g. Vink et al. 2011). This is the reason why most theoretical studies of pair instability supernovae (PISNe) have focused

on zero or extremely metal poor stars in the early Universe (El Eid et al. 1983; Umeda & Nomoto 2002; Heger & Woosley 2002; Scannapieco et al. 2005; Kasen et al. 2011; Pan et al. 2012a; Whalen et al. 2013a; Dessart et al. 2013). However, Langer et al. (2007) recently pointed out that the metallicity threshold for PISNe can be as high as $Z_{\odot}/3$ within the current theoretical uncertainty of stellar wind mass-loss rates, implying one PISN per one thousand supernovae in the local Universe.

PISNe would be marked by broad light curves given their high progenitor masses. They would also appear extremely luminous if their progenitors have large radii and/or if a large amount of nickel is produced as a result of the pair creation instability (e.g., Scannapieco et al. 2005; Kasen et al. 2011). This raises the question whether some of the super-luminous SNe of various types like SN 2006gy and SN 2007bi discovered in the nearby Universe have a pair instability origin (see Gal-Yam 2012, for a review). For example, the light curve of SN 2007bi implies the radioactive decay of more than $3 M_{\odot}$ of nickel, for which a pair instability explosion gives one of the best explanations (Gal-Yam et al. 2009). Alternative possibilities are supernova powered by a young magnetar as suggested by various authors (Kasen & Bildsten 2010; Dessart et al. 2012) and interaction-driven supernova (Moriya et al. 2010). If local PISNe would exist, one would have to wonder how they would have impacted on the chemical evolution of the local Universe.

Addressing these questions requires PISN models that are relevant to the environment of the local Universe. The first studies of local PISN models were performed by Langer & El Eid (1986), El Eid & Langer (1986) and Herzig et al. (1990) who calculated evolutionary models with an initial mass of $100 M_{\odot}$ and a metallicity of $Z = 0.03$. More recently, Langer et al. (2007) calculated $150 M_{\odot}$ and $250 M_{\odot}$ models at a metallicity of $Z = 0.001$ as PISN progenitors, adopting the most up-to-date prescriptions for stellar wind mass-loss rates. These models provide self-consistent progenitor models for PISNe in the local Universe together with more recent models by Yusof et al. (2013). In the present study we follow the evolution of two models from Langer et al. (2007) through the explosive oxygen and silicon burning stages to verify that they explode via the pair instability mechanism, and to discuss implications for nucleosynthesis in the local Universe. Their shock-breakout signatures and light curves will be discussed in a separate paper (Kozyreva et al. 2014).

This paper is organized as follows. We describe the numerical method adopted in the present study in Section 2. The results of our calculations are reported in Section 3, where we also discuss the nucleosynthesis yields of our PISN models. We discuss the implications of our results for the chemical evolution of the local Universe in Section 4, and conclude our study in the final section.

2. Numerical method and input physics

We use an implicit Lagrangian hydrodynamics code which solves the difference equations for the stellar structure iteratively by the Henyey relaxation method (Henyey et al. 1964; Heger et al. 2000; Yoon & Langer 2005; Yoon et al. 2006). We list the relevant stellar structure equations in the Appendix A. The equation of state is based on Blinnikov et al. (1996) and includes ions, electrons and positrons, radiation, degeneracy effects and ionization contributions. The opacity is computed from the OPAL tables (Iglesias & Rogers 1996) and Alexander & Ferguson (1994).

We compute the nucleosynthesis and the corresponding energy generation rate in the following way. For temperatures less than 4.5×10^8 K, a small nuclear network (39 isotopes) is utilized. For higher temperatures we use the ‘‘Torch’’ nuclear network developed by Timmes (1998, 1999) with 200 isotopes. In this network, the weak interactions are followed using the data provided by Fuller et al. (1982). For a temperature range where silicon burning is well described in terms of quasi-statistical equilibrium (QSE, Bodansky et al. 1968; Hix & Thielemann 1996), energy generation rates can be given as a function of temperature T , density ρ , total mass fraction of the silicon QSE-group¹ elements X_{Si} and electron abundance Y_e . For calculating energy generation rates during silicon burning, therefore, we use an energy generation rate table for a number of combinations of different physical parameters ($T = (2.4 - 5) \times 10^9$ K, $\log_{10}(\rho / (\text{g cm}^{-3})) = 5 - 10$, $X_{\text{Si}} = 0 - 1$, $Y_e = 0.44 - 0.5$), following Nomoto & Hashimoto (1988). For very high temperatures ($T > 5 \times 10^9$ K), the nuclear statistical equilibrium routine by Timmes (1998) is employed.

Our starting models are taken from the stellar evolutionary calculations with an initial masses of $150 M_{\odot}$ and $250 M_{\odot}$ and initial rotational velocity of 10 km s^{-1} at $Z = 0.001$ by

¹ QSE-groups are the groups of isotopes formed in the condition of quasi-statistical equilibrium (Wallerstein et al. 1997).

Langer et al. (2007, the model Sequences 3 and 4). These models were calculated from the zero-age main sequence until the onset of the pair instability in the core, with the stellar wind mass-loss prescription described in Yoon et al. (2006). The starting point of our calculations is core carbon exhaustion, after which these stars quickly enter the pair instability phase. The stellar masses at this point are $94 M_{\odot}$ and $169 M_{\odot}$ for the $150 M_{\odot}$ and $250 M_{\odot}$ stars, respectively. We summarize some model properties in Table 1 along with those of zero metallicity models by Heger & Woosley (2002) for comparison.

The stellar evolutionary models from Langer et al. (2007) were calculated using the Ledoux criterion for convection, with the assumption of semi-convection (Langer et al. 1983) using a large semi-convective mixing parameter ($\alpha_{\text{SEM}} = 1$, Langer (1991)), and without convective core overshooting. The mixing length parameter was chosen to be 1.5 of pressure scale height (Yoon et al. 2006). We neglected the convective mixing during the explosive oxygen and silicon burning phases in our calculations because the convection timescale is two orders of magnitude larger than the hydrodynamical timescale on which the collapse induced by the pair instability develops.

Note that the recent PISN progenitor models at higher metallicity (0.002 and 0.006) by Yusof et al. (2013) are computed using the Schwarzschild criterion for convection and with core overshooting with a moderate overshooting parameter ($\alpha_{\text{over}} = 0.1$). The convection in the outer layers is calculated with mixing-length parameter scaled to the density scale height ($\alpha_{\text{MLT}} = l/H_{\rho} = 1$) to avoid density inversions (see also Ekström et al. 2012). The consequences of this treatment are more compact stellar models, a lesser degree of mass loss, and larger carbon-oxygen cores. Those models from Yusof et al. (2013) which are supposed/declared to produce PISNe are evolved until the end of helium/oxygen burning. Electron-positron pair creation is not included in the equation of state of the employed evolutionary code. The statement about the PISN fate is based on the size of the carbon-oxygen core. In more recent study the PISN models from Yusof et al. (2013) (at the end of core helium burning) were mapped into the KEPLER code (Heger & Woosley 2010). With these calculations the models were evolved through pair instability and eventually exploded (Whalen et al. 2013b).

Rotation is not included during the present calculations because these models retain very small amounts of angular momentum.

3. Results

3.1. Explosion

Through the hydrodynamics terms included in the BEC code (see the Appendix A) we could follow the dynamical phase of the evolution of our PISN models. Usually hydrodynamic stellar evolution codes are not able to describe dynamical processes in stars because of the implicit nature of the adopted numerical solvers (causing strong numerical damping) and the large time steps which are required to follow the evolution time scale (Appenzeller 1970; Woosley & Weaver 1982). Pulsations and shock waves however can be resolved if the time step becomes comparable to the dynamical characteristic time (possible during late stages of stellar evolution), and if the growth rate of a hydrodynamical phenomenon is sufficiently large (El Eid & Langer 1986; Heger et al. 1997; Yoon & Cantiello 2010).

Table 1: Properties of our PISN progenitor models and of comparable Population III helium star models from Heger & Woosley (2002). T_c^{\max} and ρ_c^{\max} are the maximum values of central temperature and central density, respectively, that are achieved during the calculations. The last two columns give the values of the central neutron excess initially and at maximum temperature.

Initial mass	Final mass	He-core	O-core	T_c^{\max}	$\log \rho_c^{\max}$	η_c^{init}	η_c^{\max}
	$[M_\odot]$	$[M_\odot]$	$[M_\odot]$	$[10^9 \text{ K}]$	$[\text{g cm}^{-3}]$		
150 M_\odot	94	72	64	3.45	6.25	1.0×10^{-4}	2.5×10^{-4}
70 M_\odot He	70	70	60	3.57	6.30	1.9×10^{-7}	2.8×10^{-4}
250 M_\odot	169	121	110	5.12	6.69	1.0×10^{-4}	1.6×10^{-3}
115 M_\odot He	115	115	90	5.14	6.67	1.9×10^{-7}	7.3×10^{-4}

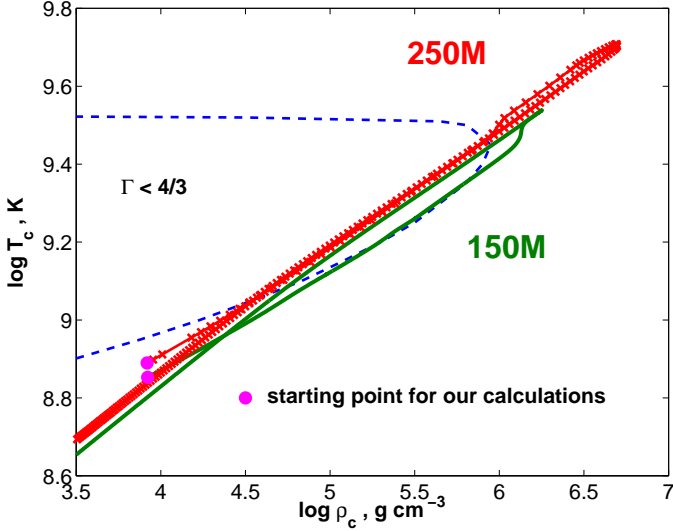


Fig. 1: Evolutionary tracks of our 150 M_\odot (labeled ‘150M’, solid line) and 250 M_\odot (labeled ‘250M’, line with times signs) models in central density – temperature diagram. The area enclosed with the dashed line indicates the pair instability regime where $\Gamma < 4/3$. The filled circles mark the starting points for each model sequence.

We find that both models explode as a result of explosive nuclear burning during the pair instability phase, which confirms the prediction by Langer et al. (2007).

In Figure 1, the evolutionary tracks of the central density and temperature are shown. Both quantities increase rapidly during the dynamical contraction of the core induced by the pair instability. The maximum temperature and density achieved during this phase are $T_c = 3.45 \times 10^9 \text{ K}$ and $\rho_c = 1.8 \times 10^6 \text{ g cm}^{-3}$ for the 150 M_\odot star, and $T_c = 5.1 \times 10^9 \text{ K}$ and $\rho_c = 4.9 \times 10^6 \text{ g cm}^{-3}$ for the 250 M_\odot star, respectively. As shown in Table 1, these values are comparable to those found in Population III star models by Heger & Woosley (2002) for similar helium core masses. Beyond this point, the contraction is reversed, and the star explodes.

In Figure 2, the fact that our models explode by the nuclear energy release is illustrated. Initially our models have a negative binding energy ($E_{\text{bind}} = E_{\text{grav}} + E_{\text{thermal}}$). The pair creation triggers the collapse which is visible as a minor increase of the kinetic energy around $t = 0$ for Model 150M and around $t = 0 - 10 \text{ s}$ for Model 250M. The consequent oxygen and silicon burning occur with a sharp decrease of the nuclear binding energy.

The nuclear binding energy is defined the following way:

$$E_{\text{bind}} = \sum_k \sum_i X_i e_i \frac{\Delta M_k}{m_i}, \quad (1)$$

where X_i represents the mass fractions of the isotopes, e_i and m_i are the nuclear binding energy and nuclear mass of the isotope i , and ΔM is the mass of the mass shell of the numerical stellar model. The sum is made over all mass shells and over all isotopes. Figure 2 shows the difference of nuclear binding energy at a given time to that at the end of carbon burning, i.e. the first time point in the figures. The drop in the nuclear binding energy shows the amount of energy released by nuclear burning during the pair instability explosion.

The released nuclear energy from oxygen and silicon burning is converted into thermal and kinetic energy, resulting in a positive binding energy. A positive binding energy means that the system becomes unbound. Eventually, most of the released nuclear energy is converted into the kinetic energy, which is strong evidence for the explosion of the star. The final kinetic energy is 8 foe² for Model 150M and 44 foe for Model 250M. This corresponds to an asymptotic velocity of the ejecta at the infinity of $2.9 \times 10^3 \text{ km s}^{-1}$ for Model 150M and $5.1 \times 10^3 \text{ km s}^{-1}$ for Model 250M.

The BEC code has no provision for treating shocks. However, due to the strong density contrast at the base of the hydrogen-rich envelope, a shock wave develops at this point due to the explosion of the carbon-oxygen core. Its Mach number is about 2 for both our models. As a consequence, energy is not perfectly conserved in our models at the time when the shock enters the stellar envelope (see Figure3). Still the total energy is conserved to better than 5% in our 150 M_\odot model, and to better than 20% in our 250 M_\odot model. We note that the velocities scale with $\sqrt{E_{\text{kin}}}$, and that we expect our velocities to be precise to 3% and 10%, respectively. The comparison of Figures 2 and 3 shows that energy conservation during the nuclear burning phase is very good, such that our nucleosynthesis results are not affected by this issue.

3.2. Nucleosynthesis

Figure 4 shows the final chemical structure of our models. The total amounts of produced ^{56}Ni are 0.04 M_\odot and 19.3 M_\odot for the 150 M_\odot and 250 M_\odot star, respectively. As shown in Table 2, the overall nucleosynthetic results are in good agreement with that of the 70 M_\odot and 115 M_\odot Population III helium star models by Heger & Woosley (2002) of which the masses are comparable to the He core masses of our models.

² 1 foe = 10^{51} erg (from ‘fifty-one-erg’)

Table 2: Total nucleosynthetic yields for selected isotopes in solar masses for our $150 M_{\odot}$ and $250 M_{\odot}$ models (including matter lost by stellar wind and decay products) in comparison with $70 M_{\odot}$ and $115 M_{\odot}$ zero metallicity helium star yields (Heger & Woosley 2002), respectively. Yields for hydrogen and helium neglecting the wind matter are given after the slash sign.

	Z	^1H	^4He	^{12}C	^{16}O	^{20}Ne	^{24}Mg	^{28}Si	^{32}S	^{36}Ar	^{40}Ca	^{46}Ti	^{50}Cr	^{56}Fe
$150 M_{\odot}$	0.001	36.6/4.9	49.2/24.4	2.2	46.9	2.6	2.3	6.2	2.8	0.5	0.5	10^{-4}	10^{-4}	0.04
He $70 M_{\odot}$	0	-	1.5	4.5	45.8	4.0	3.0	8.0	2.4	0.3	0.2	10^{-4}	10^{-4}	0.01
$250 M_{\odot}$	0.001	57.1/10.3	81.5/47.5	0.9	42.	1.8	2.5	23.1	14.3	2.9	2.8	10^{-4}	10^{-4}	19.4
He $115 M_{\odot}$	0	-	1.8	3.7	40.	3.8	4.5	25.7	11.8	1.9	1.6	10^{-5}	10^{-4}	19.0

Table 3: Total nucleosynthetic yields in solar masses and production factors for our $150 M_{\odot}$ and $250 M_{\odot}$ models. Yields include matter lost by the stellar wind and decay products.

	Yields [M_{\odot}]		Prod. factor			Yields [M_{\odot}]		Prod. factor	
	$150 M_{\odot}$	$250 M_{\odot}$	$150 M_{\odot}$	$250 M_{\odot}$		$150 M_{\odot}$	$250 M_{\odot}$	$150 M_{\odot}$	$250 M_{\odot}$
^1H	36.56	57.10	0.34	0.32	^{41}K	1.63(-4)	3.15(-4)	3.63	4.22
^2H	7.10(-11)	1.63(-10)	1.71(-8)	2.36(-8)	^{40}Ca	0.49	2.80	45.99	156.82
^3He	5.01(-5)	5.47(-5)	9.80(-3)	6.42(-3)	^{42}Ca	1.87(-4)	2.09(-4)	2.50	1.67
^4He	49.16	81.53	1.20	1.19	^{43}Ca	6.48(-8)	2.07(-5)	4.30(-3)	0.78
^6Li	4.93(-12)	2.10(-11)	4.45(-5)	1.14(-4)	^{44}Ca	1.14(-4)	9.65(-4)	0.45	2.28
^7Li	7.17(-10)	4.57(-8)	4.55(-4)	1.74(-2)	^{46}Ca	0	0	0	0
^9Be	8.77(-12)	1.88(-11)	3.01(-4)	3.88(-4)	^{48}Ca	8.71(-20)	3.92(-17)	3.50(-15)	9.45(-13)
^{10}B	2.14(-10)	4.25(-10)	1.43(-3)	1.70(-3)	^{45}Sc	4.32(-6)	1.18(-5)	0.64	1.05
^{11}B	7.17(-10)	4.58(-9)	1.07(-3)	4.10(-3)	^{46}Ti	9.23(-5)	1.14(-4)	2.29	1.69
^{12}C	2.22	0.90	6.04	1.46	^{47}Ti	3.87(-7)	2.42(-6)	1.04(-2)	3.92(-2)
^{13}C	3.58(-4)	5.60(-4)	8.00(-2)	7.52(-2)	^{48}Ti	2.02(-4)	1.69(-2)	0.54	26.96
^{14}N	4.10(-2)	7.27(-2)	0.34	0.37	^{49}Ti	1.91(-5)	4.61(-4)	0.68	9.81
^{15}N	1.17(-4)	3.37(-5)	0.25	4.31(-2)	^{50}Ti	4.23(-12)	3.35(-12)	1.53(-7)	7.29(-8)
^{16}O	46.86	41.96	47.33	25.43	^{50}V	1.63(-10)	1.65(-10)	1.04(-3)	6.28(-4)
^{17}O	1.10(-4)	1.54(-4)	0.28	0.24	^{51}V	1.93(-5)	6.42(-4)	0.30	5.98
^{18}O	1.24(-4)	4.94(-5)	5.57	1.33(-2)	^{50}Cr	2.43(-4)	1.02(-3)	1.98	4.99
^{19}F	3.76(-7)	4.03(-7)	5.36	3.45(-3)	^{52}Cr	1.62(-3)	0.38	0.66	91.77
^{20}Ne	2.58	1.85	14.69	6.32	^{53}Cr	1.79(-4)	1.40(-2)	0.63	29.60
^{21}Ne	4.17(-4)	8.79(-5)	0.95	0.12	^{54}Cr	1.09(-8)	2.02(-8)	1.51(-4)	1.69(-4)
^{22}Ne	1.19(-3)	1.17(-3)	8.42(-2)	4.94(-2)	^{55}Mn	1.00(-3)	5.73(-2)	0.45	15.59
^{23}Na	1.39(-2)	8.67(-3)	2.39	0.90	^{54}Fe	2.12(-2)	0.21	1.82	11.07
^{24}Mg	2.30	2.52	27.12	17.83	^{56}Fe	4.62(-2)	19.33	0.24	61.36
^{25}Mg	1.34(-2)	5.37(-3)	1.20	0.29	^{57}Fe	4.41(-4)	0.21	9.93(-2)	28.38
^{26}Mg	2.68(-2)	1.11(-2)	2.09	0.52	^{58}Fe	4.09(-6)	5.44(-5)	6.81(-3)	5.44(-2)
^{27}Al	1.14(-2)	4.20(-2)	1.15	2.53	^{59}Co	3.99(-5)	5.11(-3)	6.63(-2)	5.10
^{28}Si	6.17	23.08	54.52	122.29	^{58}Ni	1.83(-3)	0.37	0.22	26.73
^{29}Si	4.62(-2)	3.24(-2)	7.76	3.26	^{60}Ni	1.24(-4)	7.35(-2)	3.75(-2)	13.36
^{30}Si	2.52(-2)	1.35(-2)	6.19	2.00	^{61}Ni	2.57(-7)	3.75(-3)	1.76(-3)	15.44
^{31}P	2.96(-3)	8.16(-3)	2.60	4.30	^{62}Ni	9.40(-7)	2.59(-2)	1.99(-3)	32.86
^{32}S	2.82	14.32	47.47	144.69	^{64}Ni	7.44(-12)	4.46(-9)	6.00(-8)	2.16(-5)
^{33}S	3.83(-3)	8.14(-3)	7.93	10.11	^{63}Cu	3.95(-9)	2.40(-5)	3.92(-5)	0.14
^{34}S	8.17(-3)	1.12(-2)	2.93	2.41	^{65}Cu	1.76(-11)	9.92(-6)	3.80(-7)	0.13
^{36}S	2.36(-8)	5.23(-8)	1.96(-3)	2.62(-3)	^{64}Zn	1.98(-9)	1.20(-4)	1.18(-5)	0.43
^{35}Cl	7.24(-4)	1.09(-2)	1.19	10.70	^{66}Zn	6.34(-11)	2.24(-4)	6.40(-7)	1.36
^{37}Cl	6.68(-4)	1.37(-3)	3.25	4.01	^{67}Zn	5.63(-15)	1.56(-7)	3.81(-10)	6.34(-3)
^{36}Ar	0.51	2.93	37.28	128.15	^{68}Zn	8.90(-15)	4.64(-8)	1.30(-10)	4.06(-4)
^{38}Ar	6.75(-3)	7.92(-3)	2.57	1.81	^{70}Zn	0	0	0	0
^{40}Ar	1.37(-10)	3.11(-9)	3.26(-5)	4.42(-4)	^{69}Ga	4.22(-16)	4.47(-13)	6.45(-11)	4.10(-8)
^{39}K	1.23(-3)	1.16(-2)	2.09	11.82	^{71}Ga	0	0	0	0
^{40}K	3.71(-8)	1.68(-6)	3.95(-2)	1.07	^{70}Ge	6.93(-16)	9.16(-15)	8.82(-11)	7.00(-10)

We summarize the chemical yields and the production factors of each isotope from our explosion models in Table 3. Here the production factor of a given isotope is defined as

$$p_{\text{iso}} = \frac{m_{\text{iso}}}{X_{\text{iso}}^{\odot} \times M_{\text{tot}}}, \quad (2)$$

where m_{iso} is the total yield of a given isotope in solar masses, X_{iso}^{\odot} is the mass fraction of the isotope according to the solar metallicity pattern, and M_{tot} is the initial mass of the star ($150 M_{\odot}$ or $250 M_{\odot}$ in the present study). The effect of radioactive decays is fully considered in the final set of the isotope yields that consists only of stable nuclei.

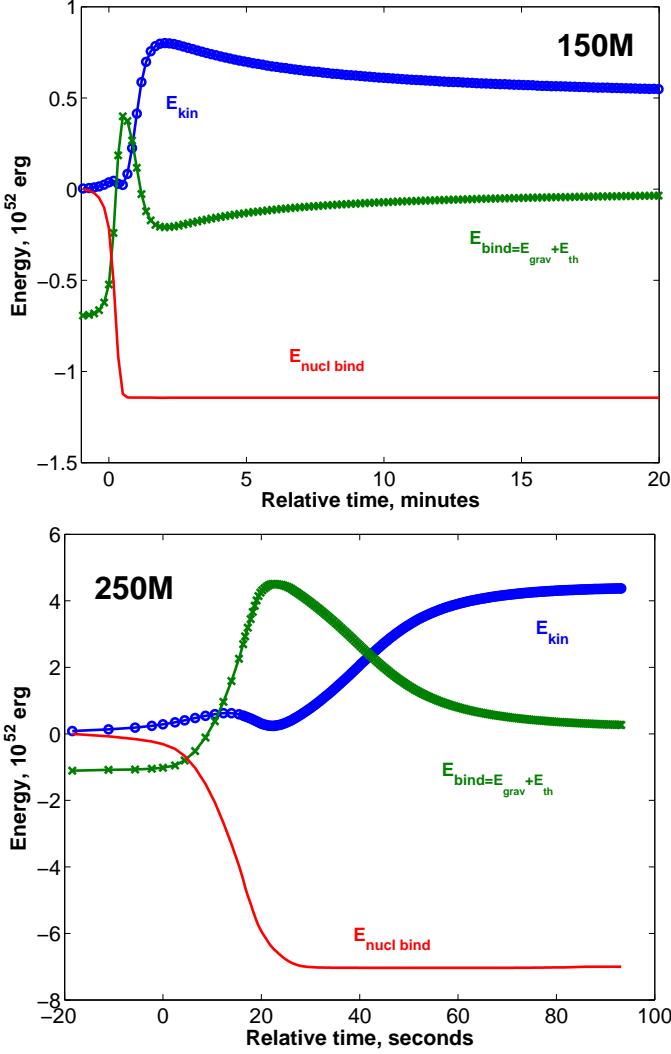


Fig. 2: Evolution of the energetics for our 150 M_{\odot} and 250 M_{\odot} models. The kinetic energy (blue, circles), the binding energy (green, times) that is the sum of gravitational and thermal energies, and the nuclear binding energy (red) of the stars are shown. Here, the nuclear binding energy is defined by the difference between the total nuclear binding energy of all nuclei at the end of carbon burning and that of a given evolutionary epoch (see description in the text). The zero point in time is defined as the time of the beginning of pair instability explosion.

We use the solar abundances taken from Woosley & Weaver (1995) which were adopted from Anders & Grevesse (1989) to be consistent in our comparison to other PISN and CCSN nucleosynthetic yields. A more recent study of solar abundances (Asplund et al. 2009) shows somewhat different solar abundances. The overall fraction of heavy elements differs by a factor of 0.7 mostly due to a reduced oxygen abundance. $Z = 0.0134$ in Asplund et al. (2009) and $Z = 0.0201$ in Anders & Grevesse (1989). However, the solar abundances serve as a denominator for our qualitative comparison. Generally, the relative scatter of the elemental/isotopic production factor (i.e. odd-even effect) remains the same. We plot all production factors in Figures 6, 7, and 9 in logarithmic scale. Therefore, using the lower metal fraction will shift all data (except hydrogen and helium) by $|\log 0.7| \approx 0.15$ dex.

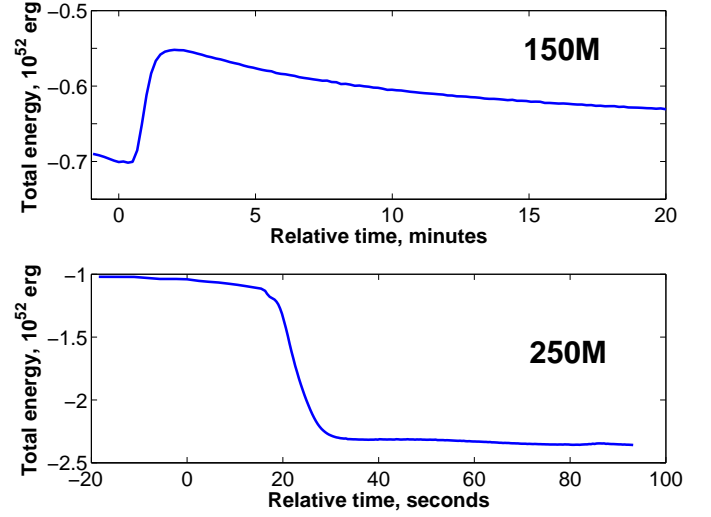


Fig. 3: Total energy evolution for our 1500 M_{\odot} (upper) and 250 M_{\odot} (bottom) models.

The pair instability explosion in our models is mostly driven by oxygen burning because oxygen is the most abundant element at core carbon exhaustion. Our models 150M and 250M contain 64 M_{\odot} and 110 M_{\odot} oxygen cores, correspondingly, and a large fraction of the oxygen core remains unburnt: more than 40 M_{\odot} of oxygen enrich the circumstellar medium, making oxygen the third most abundant element after hydrogen and helium. Note that only about 3 M_{\odot} of oxygen are produced in an ordinary core-collapse SN (Woosley & Weaver 1995) and even less (about 0.1 M_{\odot}) is left after a SN Ia (Iwamoto et al. 1999; Travaglio et al. 2004).

The highest yields in Model 150M are those of intermediate even-charged isotopes between oxygen and sulphur (2.6 M_{\odot} of ^{20}Ne , 2.3 M_{\odot} of ^{24}Mg , 6.2 M_{\odot} of ^{28}Si , 2.8 M_{\odot} of ^{32}S) because only a small fraction of silicon is burnt in this PISN (see Table 3). The yields of iron-group isotopes are fairly low compared to intermediate mass isotopes. At the same time the ejecta of Model 250M contains large amounts of intermediate mass isotopes similar to the Model 150M (1.85 M_{\odot} of ^{20}Ne , 2.5 M_{\odot} of ^{24}Mg , 23.1 M_{\odot} of ^{28}Si , 14.3 M_{\odot} of ^{32}S , 2.9 M_{\odot} of ^{36}Ar , 2.8 M_{\odot} of ^{40}Ca), significant amounts of iron-group isotopes (0.4 M_{\odot} of ^{52}Cr , 0.2 M_{\odot} of ^{54}Fe , 0.2 M_{\odot} of ^{57}Fe , 0.4 M_{\odot} of ^{58}Ni) and a very large iron-56 yield (19.3 M_{\odot}). There is a gap around the titanium isotopes since these are the bottle-neck isotopes between QSE-groups (Hix & Thielemann 1996).

Large amounts of silicon (6 M_{\odot} and 23 M_{\odot} , respectively) are left after incomplete silicon burning in both models, which are 10 – 100 times higher than silicon yields resulting from core-collapse SNe and SNe Ia. The average yield of silicon in core-collapse SNe and SNe Ia is 0.4 M_{\odot} and 0.6 M_{\odot} , respectively. A large amount of radioactive nickel produced in our higher mass Model 250M (19.3 M_{\odot}) will result in a very bright and broad supernova light curve (Scannapieco et al. 2005; Kasen et al. 2011; Kozyreva et al. 2014). This amount is much larger than the average iron yield of 0.04 – 0.2 M_{\odot} in core-collapse SNe and 0.5 M_{\odot} in SNe Ia (Patat et al. 1994; Smartt 2009).

We emphasize here that both our PISN models do not produce pronounced amounts of isotopes beyond the iron-group: the mass fractions of copper, zinc gallium and germanium isotopes

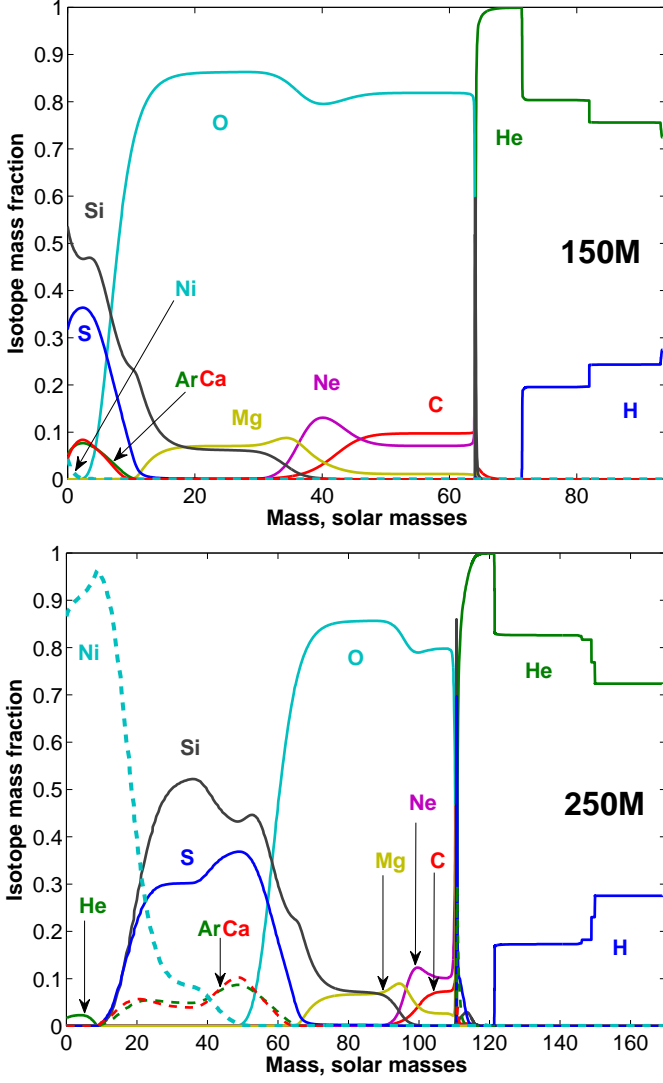


Fig. 4: The final chemical structure of our models.

are well below 10^{-4} . The lack of r - and s -isotopes is explained mostly by the neutron deficiency that is explained below³.

PISNe occur since the cores of their progenitors remain much less dense than those of core-collapse SN progenitors (c.f. Langer 2012). This makes neutronization during the final evolutionary stages much less significant than in core-collapse progenitors. Heger & Woosley (2002) showed that this results in a remarkable deficiency of odd-charged nuclei compared to even-charged nuclei in the nucleosynthesis of Population III PISNe. Table 1 shows that our starting models have much larger neutron excesses ($\eta_i \sim 10^{-4}$) than the initial Population III star models of Heger & Woosley ($\eta_i \sim 10^{-7}$). However, the neutron excess in the central region (η_c) where silicon burning occurs does not increase much. The maximum neutron excess achieved at the center (η_c^{\max}) in the $150 M_{\odot}$ and $250 M_{\odot}$ models is only 2×10^{-4} and 1.6×10^{-3} , respectively. In the comparable Population III helium star models of Heger & Woosley (2002) (i.e. their $70 M_{\odot}$ and $115 M_{\odot}$ models; see Figure 2), the values of η_c^{\max} are 2.8×10^{-4} and 7.3×10^{-4} , respectively (Table 1), which is a factor of 3...5 lower.

³ Note that in the nuclear network used in our study no element heavier than germanium is included.

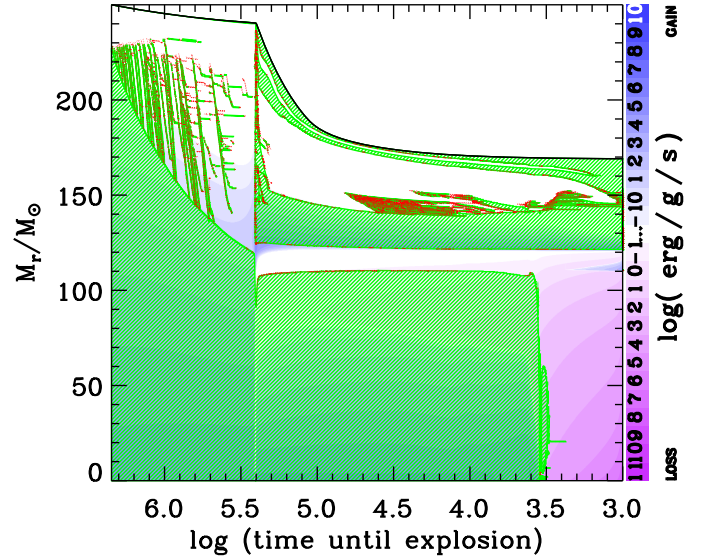


Fig. 5: Kippenhahn diagram for the $250 M_{\odot}$ PISN model. Convective and semi-convective layers are marked by green hatched lines and red dots, respectively. The net amount of local energy loss and production is indicated by color shading. The surface of the star is marked by the black solid line.

This indicates that the neutron excess in PISNe during the explosion phase does not increase by much more than about 10^{-3} over the values at core helium exhaustion. Interestingly, this implies that even if the initial metallicity of a PISN progenitor was as high as Z_{\odot} , the neutron excess in the core would not become much higher than about 10^{-3} , which is the typical value of the neutron excess in the innermost layers of solar metallicity massive stars at core helium exhaustion. This value is much smaller than the neutron excess achieved in the silicon shell of a typical core-collapse progenitor ($\eta \approx 10^{-2}$), where explosive nuclear burning occurs during the supernova explosion. We conclude that the odd-even effect is expected to be significant even in metal-rich PISNe.

Heger & Woosley (2005) argued that an unusually strong mixing of nitrogen into the helium core of a PISN progenitor may make the odd-even effect as weak as in the nucleosynthesis of a core-collapse supernova. However, to increase the neutron excess to $\eta \approx 10^{-2}$ by such mixing is very difficult to achieve in massive stars, as discussed in Yoon et al. (2012). It requires abundant production of primary nitrogen in the first place, which in turn requires efficient chemical mixing of carbon and oxygen into hydrogen shell burning during the post-main sequence phases. Then, the primary nitrogen has to be mixed into the core of the star to increase the neutron excess, via the $^{14}\text{N}(\alpha, \gamma)^{18}\text{F}(e^+, \nu)^{18}\text{O}$ reaction. One possibility for such mixing is the penetration of the helium-burning convective core into the hydrogen burning shell source, which is often observed in massive Population III star models (Heger & Woosley 2010; Yoon et al. 2012). Such mixing of nitrogen into the stellar core by convection is not observed in our PISN progenitor models as shown in Figure 5. Even if it occurred, it would be difficult to enhance the neutron excess to more than about 10^{-3} (Yoon et al. 2012). Another possibility is rotationally induced mixing. Our models are initially slow rotators and lost most of their initial angular momentum via mass loss, rendering the role of rotation unimportant. Yoon et al. (2012) concluded that mixing of nitrogen resulting from rotation may not enhance the neutron

excess by more than about 10^{-5} even for the extreme case of the so-called chemically homogeneous evolution. Furthermore, PISNe through chemically homogeneous evolution are expected only at extremely low metallicity of $Z \lesssim 10^{-5}$ (Yoon et al. 2006; Langer et al. 2007). We conclude that the neutron excess does not exceed $\sim 10^{-3}$ in most PISN progenitors.

As expected from the above discussion, the odd-even effect in our models also appears to be strong (Figures 6, 7, and 9). The ratio of the even- to odd-charged isotope mass fractions reaches $10^2 - 10^5$, which is far from the observed values in the solar system and in metal-poor stars (Cayrel et al. 2004; Christlieb et al. 2004; Frebel et al. 2005). However, this effect is significantly weakened, compared to the case of the corresponding Population III star models, for relatively light nuclei (i.e., lighter than silicon for the $150 M_{\odot}$ model and calcium for the $250 M_{\odot}$ model respectively). This is because these elements are produced in the upper layers of the star where neutronization during the explosive phase does not occur and the degree of the odd-even effect is largely determined by the initial metallicity of the star. For example, the production factors of magnesium and sodium differ by 1.2 dex in our $250 M_{\odot}$ model, while this difference increases to 2.1 dex in the corresponding Population III model.

Note also that the overall production factors of our models are smaller than those of the corresponding Population III star models, despite the fact that the total yields of heavy elements are similar as shown in Table 2. For example, the production factors of iron from our $250 M_{\odot}$ model and a Population III $115 M_{\odot}$ helium star model are 59 and 125, respectively, while both models give the same total amount of iron (about $19 M_{\odot}$). The reason for this difference is simply that the presence of a hydrogen envelope is ignored in the case of the Population III helium star models (i.e., the helium core masses correspond to the initial masses), while in our models the helium core masses are only certain fractions of the initial masses.

In the next section, we discuss the implications of this result for the chemical evolution of galaxies.

4. Implications for chemical evolution

As mentioned above, very massive stars at relatively high metallicity are supposed to lose too much mass to produce PISNe, and metal-poor environments are preferred for PISN progenitors. Langer et al. (2007) argued that the metallicity threshold for PISNe (Z_{PISN}) may be about $Z_{\odot}/10 \dots Z_{\odot}/3$. This conclusion is in an agreement with the recent result of another detailed numerical study by Yusof et al. (2013).

Therefore, it is an important question how PISNe contributed to the chemical evolution of galaxies in environments with $Z \lesssim Z_{\text{PISN}}$. This critically depends on how many PISN progenitors form as a function of time. There are several possibilities for the formation mechanism of very massive stars (cf. Zinnecker & Yorke 2007), including very rapid mass accretion (e.g. Hosokawa & Omukai 2009), mergers in close binary systems and stellar collisions (e.g., Yungelson et al. 2008; Pan et al. 2012b). Recent observations indicate that the upper stellar mass limit (M_{UP}) may be as high as $180 M_{\odot}$ in our Galaxy and $300 M_{\odot}$ in Large Magellanic Cloud (Crowther et al. 2010; Schneider et al. 2014). Because of the paucity of very massive stars discovered in the local Universe, these observations still do not give a good constraint on the initial mass function for potential progenitors of PISNe. If we simply assume the Salpeter-like IMF ($\Gamma = -2.3$), about 2% of all supernova progenitors

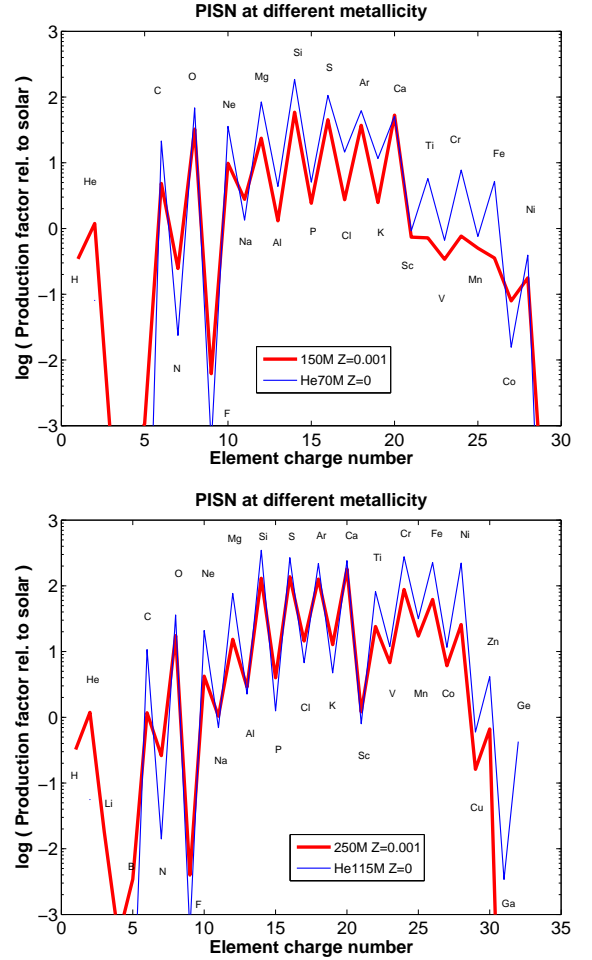


Fig. 6: Production factors of major elements from our $150 M_{\odot}$ (upper panel) and $250 M_{\odot}$ (lower panel) PISN models (red thick lines) compared with those of comparable $70 M_{\odot}$ (upper panel) and $115 M_{\odot}$ (lower panel) Population III helium star model by Heger & Woosley (2002) (blue thin lines).

($M \gtrsim 12 M_{\odot}$) have initial masses high enough ($M \gtrsim 140 M_{\odot}$) to produce a PISN.

To evaluate the contribution of PISNe to chemical evolution compared to that of core-collapse SNe, we calculated the production factor of major nuclei in the following way. The production factor integrated over an IMF ($\Phi(M) \propto M^{\Gamma}$) relative to solar abundances for a given isotope is given by

$$p_{\text{int}} = \frac{\int_{12}^{260} m_{\text{iso}} \Phi(M) dM}{\int_{12}^{260} X_{\text{iso}}^{\odot} M \Phi(M) dM} = \frac{\int_{12}^{260} m_{\text{iso}} M^{\Gamma} dM}{\int_{12}^{260} X_{\text{iso}}^{\odot} M^{\Gamma+1} dM}. \quad (3)$$

Here, the minimum and the maximum masses for supernova progenitors are assumed to be $12 M_{\odot}$ and $260 M_{\odot}$, respectively. We adopt the core-collapse SN yields from Woosley & Weaver (1995). Since we have only two models at $150 M_{\odot}$ and $250 M_{\odot}$, we interpolate and extrapolate our results to cover the full PISN regime ($140 - 260 M_{\odot}$) for this calculation, as shown in Figure 8. From the qualitative analysis of metal-free helium PISN models (Heger & Woosley 2002) we find that linear interpolation gives about 20% effect on weighted bulk yields, which correspond to 0.1 – 0.2 dex differences for final bulk production factors.

This figure illustrates the contributions of core-collapse SNe and PISNe to the chemical enrichment. We assume that yields

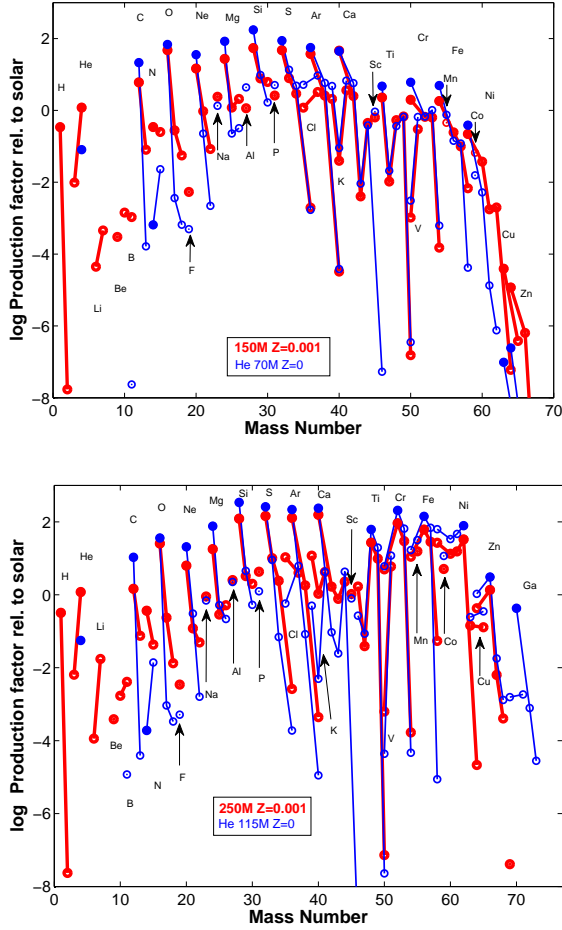


Fig. 7: Isotopic production factors for the indicated nuclei. The isotopes of a given element are connected by solid lines. The filled circles indicate the most abundant isotope for each element, while the open circles denote the other isotopes. Our $150 M_{\odot}$ (upper panel) and $250 M_{\odot}$ (lower panel) PISN models (red thick) are compared with those of comparable $70 M_{\odot}$ (upper panel) and $115 M_{\odot}$ (lower panel) Population III helium star model by Heger & Woosley (2002) (blue thin).

from core-collapse SNe come from the explosions of massive stars in the mass range from $12 M_{\odot}$ to $40 M_{\odot}$. These values are taken from the low energy explosion models of massive stars at a metallicity of $Z = 0.002$ by Woosley & Weaver (1995). The integration over the hatched regions in the figure denotes the IMF-weighted total amount of heavy elements (all elements heavier than helium) ejected by the stars from one generation. Note that even though the number of stars in the PISN range is significantly smaller than the number of core-collapse progenitors, the total amount of heavy elements ejected from PISNe appears comparable to the integrated CCSN yield.

Here we assume that stars with initial masses between $40 M_{\odot}$ and $140 M_{\odot}$, and also above $260 M_{\odot}$ do not considerably contribute to the enrichment of surrounding medium with heavy elements. We should mention that massive stars lose mass through winds, which may be enhanced in metals (e.g. carbon) and they contribute to the galactic enrichment even though they form black holes in the end. However, the stellar winds, also those of the carbon-rich Wolf-Rayet stars, are reduced for lower initial

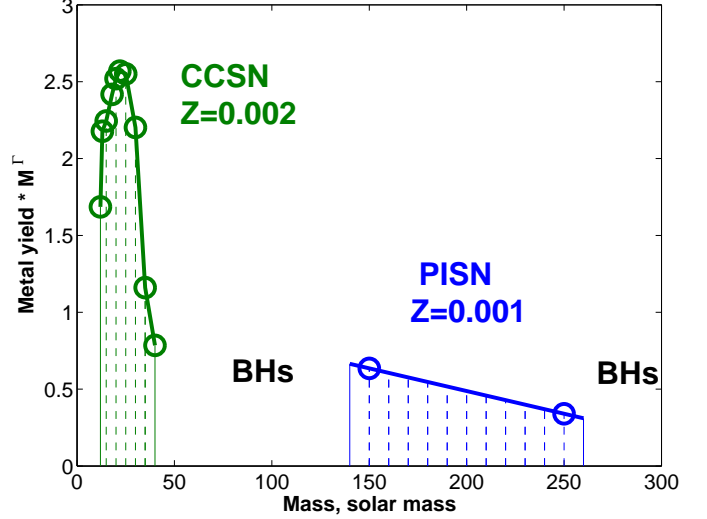


Fig. 8: The total metal yields of core-collapse SN models at $Z = 0.002$ provided by Woosley & Weaver (1995) (the A-series SNe models; green line) and of PISNe at $Z = 0.001$ (blue line), multiplied by the initial mass function probability ($\Phi(M) \propto M^{\Gamma}$), as a function of the initial mass. The y-axis is given in arbitrary units. Here, the PISN yields in the range $140 M_{\odot} - 260 M_{\odot}$ are given by the extrapolation and interpolation of our $150 M_{\odot}$ and $250 M_{\odot}$ model results. We assumed a negligible metal yield for $40 M_{\odot} < M < 140 M_{\odot}$ and above $260 M_{\odot}$.

iron abundances (Vink & de Koter 2005), such that their effect at the considered metallicities will be small.

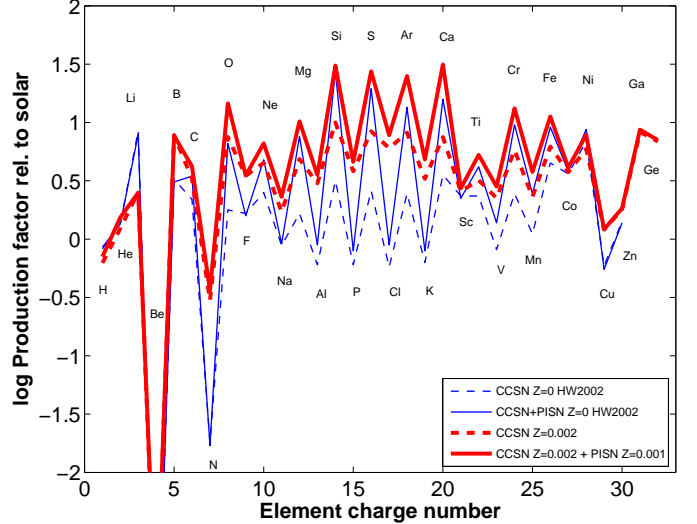


Fig. 9: Production factors relative to solar abundances of major elements from core-collapse SNe (dotted lines), and from both core-collapse and pair-instability SNe (solid lines). The blue thin lines are the results using the Population III star models by Woosley & Weaver (1995) and Heger & Woosley (2002). The red thick lines correspond to the production factors using the values from Woosley & Weaver (1995) and present study (shown in Figure 8).

Figure 9 clearly indicates that the inclusion of PISN yields has a strong impact on the total production factors even at finite metallicity: the production factor of the even-charged nuclei is enhanced by a factor of 2 – 3 for most of the α -elements with PISNe, while it is mostly negligible for the odd-charged nuclei. Note that this odd-even effect becomes strongest for the elements between Al and Sc. However, the odd-even effect is much weaker in our models compared to the Population III models. The Population III yields give almost 10 times higher production factors of even-charged nuclei with the inclusion of PISNe. This difference is mainly because the overall core-collapse SN yields at a metallicity of $Z = 0.002$ are significantly larger than those of Population III core-collapse SNe, and partly because our PISN models give a somewhat weaker odd-even effect than the Population III models as discussed above.

As discussed in Section 1, the event rate of PISNe is expected to decrease to zero for metallicities higher than about $Z = Z_{\odot}/3$. The nucleosynthetic signature of PISNe should be washed out by contribution of core-collapse SNe as the metallicity reaches the solar value, and the effect of PISNe on chemical evolution might not be found in Population I stars. However, from our study we conclude that the impact of PISNe in the environment of $Z = 0.001 - 0.002$ may be still significant depending on the IMF, and should be tested in future observations of Population II stars with metallicities well below $Z = Z_{\odot}/3$.

5. Conclusions

In the frame of this study we calculated the evolution of two very massive stellar models at a metallicity of $Z = 0.001$. These two models have initial zero age main sequence masses of $150 M_{\odot}$ and $250 M_{\odot}$. The models were evolved through the core hydrogen, helium and carbon burning (Langer et al. 2007) with the Binary Evolution Code BEC of the Bonn stellar physics group (Yoon et al. 2006). Here, we continued the evolution using the same evolutionary code with an extended nuclear network where 200 isotopes are considered. We evolved these models through the electron-positron pair creation phase and the consequent collapse and explosive oxygen and silicon burning. The $150 M_{\odot}$ and $250 M_{\odot}$ models eject a total amount of $64 M_{\odot}$ and $111 M_{\odot}$ of metals, respectively.

We find that an excess production of even-charged elements compared to odd-charged elements is still found in our models as in Population III PISNe. However, the odd-even effect is smaller for most of the α -elements compared to the case of Population III stars because of the initially higher metallicity. The nucleosynthetic pattern of the iron-group elements is critically determined by the neutronization during the explosive burning and therefore less affected by the initial metallicity.

Given that our $150 M_{\odot}$ and $250 M_{\odot}$ models represent the low-mass and high-mass ends of PISN regime respectively, this study allowed us to compare the PISN nucleosynthesis with that of core-collapse supernovae at a similar metallicity. We find that the impact of PISNe on the overall nucleosynthetic pattern is expected to be weaker at $Z = 0.001 - 0.002$ than in the metal-free environment (Figure 9). This is mainly because of the higher initial neutron excess of our models set by higher initial metallicity.

However, the total nucleosynthetic yields from both core-collapse SNe and PISNe at $Z = 0.001 - 0.002$, assuming a Salpeter IMF, would result in the enhancement of α -elements by factors of 2 – 3 compared to the case without PISN contribution (Figures 8 and 9). This analysis shows that PISNe at a metallicity of $Z = 0.001$ can contribute to the enrichment of the interstellar medium with heavy elements in a similar way as Population III

PISNe: the odd-even effect is still expected in metal-poor stars at metallicities of about 0.001 – 0.002, although its degree would be reduced by factors of 3 – 4 compared to the prediction from Population III stars, as shown in Figure 9. Therefore, our models may be a useful guide for interpreting future observations of the chemical abundances in Population II stars at $Z \approx 0.001 - 0.002$ to constrain the number of PISNe that might have occurred in our Galaxy.

Acknowledgements. AK thanks Dr. Sergey Blinnikov and Prof. Dr. Alexander Heger for fruitful and helpful discussions. We also thank the referee for useful comments which helped us to improve the draft.

References

- Alexander, D. R. & Ferguson, J. W. 1994, *ApJ*, 437, 879
 Anders, E. & Grevesse, N. 1989, *Geochim. Cosmochim. Acta*, 53, 197
 Appenzeller, I. 1970, *A&A*, 9, 216
 Asplund, M., Grevesse, N., Sauval, A. J., & Scott, P. 2009, *ARA&A*, 47, 481
 Barkat, Z., Rakavy, G., & Sack, N. 1967, *Physical Review Letters*, 18, 379
 Bisnovatyi-Kogan, G. S. & Kazhdan, Y. M. 1967, *Soviet Ast.*, 10, 604
 Blinnikov, S. I., Dunina-Barkovskaya, N. V., & Nadyozhin, D. K. 1996, *ApJS*, 106, 171
 Bodansky, D., Clayton, D. D., & Fowler, W. A. 1968, *ApJS*, 16, 299
 Bond, J. R., Arnett, W. D., & Carr, B. J. 1982, in *NATO ASIC Proc. 90: Supernovae: A Survey of Current Research*, ed. M. J. Rees & R. J. Stoneham, 303–311
 Cayrel, R., Depagne, E., Spite, M., et al. 2004, *A&A*, 416, 1117
 Christlieb, N., Gustafsson, B., Korn, A. J., et al. 2004, *ApJ*, 603, 708
 Crowther, P. A., Schnurr, O., Hirschi, R., et al. 2010, *MNRAS*, 408, 731
 Dessart, L., Hillier, D. J., Waldman, R., Livne, E., & Blondin, S. 2012, *MNRAS*, 426, L76
 Dessart, L., Waldman, R., Livne, E., Hillier, D. J., & Blondin, S. 2013, *MNRAS*, 428, 3227
 Ekström, S., Georgy, C., Eggenberger, P., et al. 2012, *A&A*, 537, A146
 El Eid, M. F., Fricke, K. J., & Ober, W. W. 1983, *A&A*, 119, 54
 El Eid, M. F. & Langer, N. 1986, *A&A*, 167, 274
 Fowler, W. A. & Hoyle, F. 1964, *ApJS*, 9, 201
 Fraley, G. S. 1968, *Ap&SS*, 2, 96
 Frebel, A., Aoki, W., Christlieb, N., et al. 2005, *Nature*, 434, 871
 Fuller, G. M., Fowler, W. A., & Newman, M. J. 1982, *ApJS*, 48, 279
 Gal-Yam, A. 2012, *Science*, 337, 927
 Gal-Yam, A., Mazzali, P., Ofek, E. O., et al. 2009, *Nature*, 462, 624
 Heger, A. 1998, PhD thesis, Ph.D. Dissertation, Max-Planck-Institut für Astrophysik, unpublished (1998)
 Heger, A., Fryer, C. L., Woosley, S. E., Langer, N., & Hartmann, D. H. 2003, *ApJ*, 591, 288
 Heger, A., Jeannin, L., Langer, N., & Baraffe, I. 1997, *A&A*, 327, 224
 Heger, A., Langer, N., & Woosley, S. E. 2000, *ApJ*, 528, 368
 Heger, A. & Woosley, S. 2005, in *IAU Symposium, Vol. 228, From Lithium to Uranium: Elemental Tracers of Early Cosmic Evolution*, ed. V. Hill, P. Francois, & F. Primas, 297–302
 Heger, A. & Woosley, S. E. 2002, *ApJ*, 567, 532
 Heger, A. & Woosley, S. E. 2010, *ApJ*, 724, 341
 Henyey, L. G., Forbes, J. E., & Gould, N. L. 1964, *ApJ*, 139, 306
 Henyey, L. G., Wilets, L., Böhm, K. H., Lelevier, R., & Levee, R. D. 1959, *ApJ*, 129, 628
 Herzig, K., El Eid, M. F., Fricke, K. J., & Langer, N. 1990, *A&A*, 233, 462
 Hix, W. R. & Thielemann, F.-K. 1996, *ApJ*, 460, 869
 Hosokawa, T. & Omukai, K. 2009, *ApJ*, 703, 1810
 Iglesias, C. A. & Rogers, F. J. 1996, *ApJ*, 464, 943
 Iwamoto, K., Brachwitz, F., Nomoto, K., et al. 1999, *ApJS*, 125, 439
 Kasen, D. & Bildsten, L. 2010, *ApJ*, 717, 245
 Kasen, D., Woosley, S. E., & Heger, A. 2011, *ApJ*, 734, 102
 Kippenhahn, R. & Weigert, A. 1990, *Stellar Structure and Evolution* (Springer-Verlag Berlin Heidelberg New York. Also *Astronomy and Astrophysics Library*), 468 pp.
 Kozyreva, A., Blinnikov, S., Langer, N., & Yoon, S.-C. 2014, *ArXiv e-prints*, 1403.5212, accepted by *A & A*
 Langer, N. 1991, *A&A*, 252, 669
 Langer, N. 2012, *ARA&A*, 50, 107
 Langer, N. & El Eid, M. F. 1986, *A&A*, 167, 265
 Langer, N., Fricke, K. J., & Sugimoto, D. 1983, *A&A*, 126, 207
 Langer, N., Norman, C. A., de Koter, A., et al. 2007, *A&A*, 475, L19
 Moriya, T., Tominaga, N., Tanaka, M., Maeda, K., & Nomoto, K. 2010, *ApJ*, 717, L83

Nomoto, K. & Hashimoto, M. 1988, *Physics Reports*, 163, 13
Pan, T., Kasen, D., & Loeb, A. 2012a, *MNRAS*, 422, 2701
Pan, T., Loeb, A., & Kasen, D. 2012b, *MNRAS*, 423, 2203
Patat, F., Barbon, R., Cappellaro, E., & Turatto, M. 1994, *A&A*, 282, 731
Rakavy, G. & Shaviv, G. 1967, *ApJ*, 148, 803
Scannapieco, E., Madau, P., Woosley, S., Heger, A., & Ferrara, A. 2005, *ApJ*, 633, 1031
Schneider, F. R. N., Izzard, R. G., de Mink, S. E., et al. 2014, *ApJ*, 780, 117
Smartt, S. J. 2009, *ARA&A*, 47, 63
Timmes, F. X. 1998, http://cococubed.asu.edu/code_pages/net_torch.shtml
Timmes, F. X. 1999, *ApJS*, 124, 241
Travaglio, C., Hillebrandt, W., Reinecke, M., & Thielemann, F.-K. 2004, *A&A*, 425, 1029
Umeda, H. & Nomoto, K. 2002, *ApJ*, 565, 385
Vink, J. S. & de Koter, A. 2005, *A&A*, 442, 587
Vink, J. S., Muijres, L. E., Anthonisse, B., et al. 2011, *A&A*, 531, A132
Wallerstein, G., Iben, Jr., I., Parker, P., et al. 1997, *Reviews of Modern Physics*, 69, 995
Whalen, D. J., Even, W., Frey, L. H., et al. 2013a, *ApJ*, 777, 110
Whalen, D. J., Even, W., Smidt, J., et al. 2013b, *ArXiv e-prints*, 1312.5360, submitted to *ApJ*
Woosley, S. E. & Weaver, T. A. 1982, in *NATO ASIC Proc. 90: Supernovae: A Survey of Current Research*, ed. M. J. Rees & R. J. Stoneham, 79–122
Woosley, S. E. & Weaver, T. A. 1995, *ApJS*, 101, 181
Yoon, S.-C. & Cantiello, M. 2010, *ApJ*, 717, L62
Yoon, S.-C., Dierks, A., & Langer, N. 2012, *A&A*, 542, A113
Yoon, S.-C. & Langer, N. 2005, *A&A*, 443, 643
Yoon, S.-C., Langer, N., & Norman, C. 2006, *A&A*, 460, 199
Yungelson, L. R., van den Heuvel, E. P. J., Vink, J. S., Portegies Zwart, S. F., & de Koter, A. 2008, *A&A*, 477, 223
Yusof, N., Hirschi, R., Meynet, G., et al. 2013, *MNRAS*, 433, 1114
Zeldovich, Y. B. & Novikov, I. D. 1971, *Relativistic astrophysics. Vol.1: Stars and relativity* (Chicago: University of Chicago Press, Translated by Eli Arlock, Ed. by K.S. Thorne and W.D. Arnett), 522 pp.
Zinnecker, H. & Yorke, H. W. 2007, *ARA&A*, 45, 481

Appendix A: Basic stellar structure equations

The structure and evolution of stars are governed by a set of partial differential equations. The following are *hydrodynamic* equations which include inertia term. However, they can be easily be converted into *hydrostatic* version while equating the inertia term with zero.

The set contains the equations of (1) continuity of mass, (2) momentum and (3) energy. Written in the vector form they are:

$$\frac{\partial \rho}{\partial t} + \nabla \cdot (\rho \mathbf{u}) = 0 \quad (\text{A.1})$$

$$\frac{\partial \rho \mathbf{u}}{\partial t} + \nabla \cdot (\mathbf{u} \otimes \rho \mathbf{u}) + \nabla p_g = 0 \quad (\text{A.2})$$

$$\frac{\partial E}{\partial t} + \nabla \cdot [\mathbf{u} (E + p_g)] = 0, \quad (\text{A.3})$$

where ρ is the gas density, \mathbf{u} its velocity, p_g the gas pressure, and E the total gas energy per unit volume, $E = \rho e_{\text{int}} + \frac{1}{2} \rho u^2$, where e_{int} is the internal energy per unit mass. \otimes denotes the outer product of two vectors giving a 3×3 tensor.

In case of a non-rotating spherically symmetric star it is appropriate to use comoving Lagrangian coordinates bound with the matter. Therefore, the above-written set of equations can be replaced by the following set:

$$\left(\frac{\partial r}{\partial m} \right)_t = \frac{1}{4\pi r^2 \rho} \quad (\text{A.4})$$

$$\left(\frac{\partial r}{\partial t} \right)_m = u \quad (\text{A.5})$$

$$\left(\frac{\partial P}{\partial m} \right)_t = \frac{Gm}{4\pi r^4} - \frac{1}{4\pi r^2} \left(\frac{\partial u}{\partial t} \right)_m \quad (\text{A.6})$$

$$\left(\frac{\partial l}{\partial m} \right)_t = \varepsilon_{\text{nuc}} + \varepsilon_\nu + \frac{P}{\rho^2} \left(\frac{\partial \rho}{\partial t} \right)_m - \left(\frac{\partial \varepsilon}{\partial t} \right)_m \quad (\text{A.7})$$

$$\left(\frac{\partial T}{\partial m} \right)_t = -\nabla \frac{GmT}{4\pi r^4 P} \left[1 + \frac{r^2}{Gm} \left(\frac{\partial u}{\partial t} \right)_m \right], \quad (\text{A.8})$$

where r is the radial distance of the shell to the centre of the star, m is the mass contained – serves as mass coordinate of the shell $m(r) = \int_0^r 4\pi r^2 \rho dr$, ρ is the density in the shell, u is the radial velocity, P is the pressure, G is the gravitational constant, l is the local luminosity, T is the temperature, ε is the internal energy per unit mass, ε_{nuc} corresponds to the energy release due to thermonuclear burning, ε_ν represents the local heat losses due to neutrino flux.

The details about this set of equations can be found, e.g., in Kippenhahn & Weigert (1990); Heger (1998).

The temperature gradient in radiative mass shells

$$\nabla \equiv \left(\frac{\partial \ln T}{\partial \ln P} \right)_t \quad (\text{A.9})$$

is given by radiative temperature gradient

$$\nabla_{\text{rad}} = \frac{3}{16\pi a c G} \frac{\kappa l P}{m T^4} \left[1 + \frac{r^2}{Gm} \left(\frac{\partial u}{\partial t} \right)_m \right]^{-1}, \quad (\text{A.10})$$

where a is the radiation constant, c is the speed of light, and κ is the Rosseland mean opacity. The opacities are based on Alexander & Ferguson (1994) and Iglesias & Rogers (1996).

The temperature gradient in convective shells is calculated using the mixing-length theory (see e.g. Kippenhahn & Weigert 1990, and references therein).

The equation of state should be added to this set of equations, which binds the pressure P with the temperature T .

The set of equations is the system of non-linear partial differential equations. The evolution code solves it using the Newton-Raphson iteration method. The details about the numerical method can be found in Henyey et al. (1959) and Henyey et al. (1964).